# Tungsten spectroscopy in the EUV range observed at a high-temperature superconducting electron-beam ion trap

Wenxian Li,[1,2] Zhan Shi,[3] Yang Yang,[1,2] Jun Xiao,[1,2] Tomas Brage,[3] Roger Hutton,[1,2,*] and Yaming Zou[1,2]

[1]*The Key Laboratory of Applied Ion Beam Physics, Ministry of Education, 200433 China*

[2]*Shanghai EBIT laboratory, Institute of Modern Physics, Fudan University, Shanghai, 200433 China*

[3]*Division of Mathematical Physics, Department of Physics, Lund University, S-22100 Sweden*

(Received 17 March 2015; published 2 June 2015)

We have recorded extreme ultraviolet spectra from $W^{11+}$ to $W^{15+}$ ions using a flat-field spectrometer installed at the Shanghai high-temperature superconducting electron-beam ion trap. The spectra were recorded at beam energies ranging between 200 and 400 eV and showed spectral lines and transition arrays in the 170–260 Å region. The charge states and spectra transitions were identified by comparison with calculations using a detailed relativistic configuration interaction method and collisional-radiative model, both incorporated in the flexible atomic code. Atomic structure calculations showed that the dominant emission arises from $5d \rightarrow 5p$ and $5p \rightarrow 5s$ transitions. The work also identified the ground-state configuration of $W^{13+}$ as $4f^{13}5s^2$ both theoretically and experimentally.

DOI: 10.1103/PhysRevA.91.062501 PACS number(s): 32.30.Jc, 31.15.ag

## I. INTRODUCTION

There has been strong interest in tungsten spectroscopy due to the potential use of this element as a plasma-facing material in the International Thermonuclear Experimental Reactor (ITER) tokamak [1,2], especially in the divertor region [3]. Spectra diagnostics of the ITER divertor region will therefore require a large amount of as yet unavailable tungsten atomic data. The ITER divertor soft x-ray spectrometer will operate in the 150–400 Å region [4], where only 108 lines are known [5]. Of these 102 lines originate from $W^{4+}$, $W^{5+}$, and $W^{6+}$. One line is identified as being from $W^{51+}$, which is too highly ionized to be observed in the divertor region. The plasma temperature in the divertor region of ITER is expected to be in the region of a few to a few hundred eV, which will result in tungsten in charge states of up to around 28+. The remaining five tungsten lines in this wavelength region are reported to be from $W^{13+}$ but might be misidentified [6]. In contrast to this, the diagnostics of the core plasma region has stronger support since considerably more spectroscopic work, both experimental and theoretical, has been reported for the important charge states (see the review by Kramida [7]).

In previous papers we have investigated visible $M1$ transitions in $W^{13+}$ [8], $W^{25+}$ [9], $W^{26+}$ [10], $W^{27+}$ [11] (with an extension to the silver isoelectronic sequence [12,13]), and $W^{28+}$ [14]. In the present work we report on a study of tungsten ions in the wavelength region of interest to ITER divertor diagnostics, i.e., 150–400 Å. Using the Shanghai high-temperature superconducting electron-beam ion trap (SH-HtscEBIT), which was designed for low-energy electron-beam operation, we observed spectra from $W^{11+}$ through $W^{15+}$. The spectra were recorded using a recently developed high-resolution flat-field spectrometer [15]. From calculations of the relevant atomic structure and also a collisional radiative model, using the flexible atomic code (FAC) [16], we have identified lines and spectral features as originating from $5d \rightarrow 5p$ and $5p \rightarrow 5s$ transitions. We will also discuss the interesting case of $W^{13+}$ in more detail due to the controversy over the classification of the ground state which has existed since the calculations by Curtis and Ellis [17].

## II. EXPERIMENTAL METHOD

The experiment was carried out using the SH-HtscEBIT, which is described elsewhere [18]. This EBIT is capable of operating in the range of electron-beam energies between 30 and 4000 eV. The magnetic field, which is created by liquid-nitrogen temperature superconducting coils, compresses the beam radius to 60 $\mu$m. The background vacuum pressure in the trap center is estimated to be lower than $10^{-10}$ Torr, which makes it possible to produce tungsten ions mainly through electron collisional ionization with negligible influence from charge exchange. The spectra were recorded by utilizing a high-resolution grazing-incidence flat-field spectrometer, which covers the range of 10 to 500 Å and reaches a resolving power above 800 [15]. In order to eliminate light from the hot cathode, a 4500-Å-thick aluminum foil was used and mounted on the window of the miniature ultrahigh vacuum gate valve between the SH-HtscEBIT and the spectrometer. Due to the aluminum $L$ absorption edge, only wavelengths longer than 171 Å can pass through this foil. For the present experiment, a Shimazdu varied-line-spacing (VLS) grating (1200 L/mm, part number 001-0659) [19–21] was used, and an Andor CCD camera (model number DO936N-00W-#BN) was placed at different positions to record different wavelength regions. Tungsten ions were obtained by injecting $W(CO)_6$, a volatile compound with a high vapor pressure at room temperature [22]. The experiments were done using electron-beam energies ranging from 200 to 400 eV in steps of about 20 eV and a beam current of 8.1 mA. The spectrometer was calibrated by several background oxygen and nitrogen lines (see Table I).

## III. DESCRIPTION OF THE CALCULATION

In order to support the identification of the recorded spectra and to predict the charge-state distributions we performed calculations using FAC version 1.1.1 [16]. This

*rhutton@fudan.edu.cn

 

TABLE I. The calibration lines used in this work from the background oxygen (O IV [23], O V [5]) and nitrogen (N IV [5], N V [5]) lines.

| | Spectra | | | | |
|---|---|---|---|---|---|
| | O V | O V | N V | N IV | O IV |
| Transition | $^1P_1$ - $^1S_0$ | $^3D_{1,2}$ - $^3P_1$ | $^2P_{1/2}$ - $^2S_{1/2}$ | $^3D_{1,2,3}$ - $^3P_2$ | $^2D_{5/2}$ - $^2P_{3/2}$ |
| Wavelength (Å) | 172.169 | 192.799 | 209.303 | 225.210 | 238.570 |

is an integrated software package [24–26] producing both structure and scattering data, including, e.g., energy levels, radiative transition rates, collisional excitation, and ionization by electron impact. FAC also includes a collisional radiative (CR) model to produce synthetic spectra for plasmas under different physical conditions. The atomic structure calculation in FAC is based on a relativistic configuration interaction (RCI) model using independent particle-basis wave functions derived from a local central potential. The orbitals are optimized in a self-consistent-field (SCF) iterative procedure. Relativistic effects are included through the Dirac-Coulomb Hamiltonian being used for the optimization. Corrections from Breit interacting and higher-order QED effects, e.g., vacuum polarization and self-energy, are included in a final CI calculation. This approach yields energy levels, radiative and autoionization rates, and collision strength from the final wave functions [24]. The CR model has been shown to be a reliable tool for the analysis of optically thin plasmas such as those in an EBIT [27]. The CR model can provide information on level populations and spectral line intensities and therefore can be used to generate synthetic spectra. In this model, we have considered electron-impact excitation and deexcitation, together with radiative transition, but neglected other effects, e.g., charge exchange and radiative recombination, since they are less important in dilute EBIT plasma. For a given excited level, with the normalization condition $\sum_i N_i = 1$, the population was obtained by solving quasistationary-state rate equations $\frac{dN_i}{dt} = 0$, where

$$\frac{dN_i}{dt} = \sum_{j\geqslant i}\left(A^r_{j\to i}N_j\right) + \sum_{j\leqslant i}\left(C^e_{j\to i}N_j\right) + \sum_{j\geqslant i}\left(C^d_{j\to i}N_j\right) - \sum_{j\leqslant i}\left(A^r_{i\to j}N_i\right) - \sum_{j\geqslant i}\left(C^e_{i\to j}N_i\right) - \sum_{j\leqslant i}\left(C^d_{i\to j}N_i\right). \tag{1}$$

In this equation $A^r_{j\to i}$, $C^e_{j\to i}$, $C^d_{j\to i}$, and $N_j$ are the radiative transition rate from level $j$ to $i$, the collisional excitation rate from $j$ to $i$, the collisional deexcitation rate from $j$ to $i$. and the population of level $j$, respectively.

Generally, the accuracy of our calculations depends on the size and completeness of the atomic model used, which is determined by the choice of included configurations. Given the complexity of tungsten ions in the range of charge states of interest here, we were forced to consider a limited number of levels in our CR model. One important consideration was to include all important metastable levels since they have long lifetimes, which in turn also gives high population, even relative to the ground state [8,14]. These properties of the metastable levels can lead to two-step excitation and ionization [14]. In $W^{6+}$ to $W^{28+}$ we will deal with configurations with open $4f$ subshells, which are known to give rise to several metastable levels due to the high angular momenta involved.

TABLE II. Configurations included in the CR model for $W^{11+}$ to $W^{15+}$ (see text), together with the resulting number of excited levels. We also give the predicted ground state of each charge state in $LS$ coupling and $jj$ coupling.

| | Ions | | | | |
|---|---|---|---|---|---|
| | $W^{11+}$ | $W^{12+}$ | $W^{13+}$ | $W^{14+}$ | $W^{15+}$ |
| Levels | 2538 | 1769 | 1196 | 3896 | 3655 |
| | $4f^{14}5s^25p$ | $4f^{14}5s^2$ | $4f^{14}5s$ | $4f^{14}$ | $4f^{13}$ |
| | $4f^{14}5s5p^2$ | $4f^{14}5s5p$ | $4f^{14}5p$ | $4f^{13}5s$ | $4f^{12}5s$ |
| | $4f^{14}5s5p5d$ | $4f^{14}5p^2$ | $4f^{14}5d$ | $4f^{13}5p$ | $4f^{12}5p$ |
| | $4f^{13}5s^25p^2$ | $4f^{14}5s5d$ | $4f^{13}5s^2$ | $4f^{13}5d$ | $4f^{12}5d$ |
| | $4f^{13}5s^25p5d$ | $4f^{14}5p5d$ | $4f^{13}5s5p$ | $4f^{12}5s^2$ | $4f^{11}5s^2$ |
| | $4f^{13}5s5p^3$ | $4f^{14}5d^2$ | $4f^{13}5p^2$ | $4f^{12}5s5p$ | $4f^{11}5s5p$ |
| | $4f^{13}5s5p^25d$ | $4f^{13}5s^25p$ | $4f^{13}5s5d$ | $4f^{12}5p^2$ | $4f^{11}5p^2$ |
| | $4f^{12}5s^25p^3$ | $4f^{13}5s^25d$ | $4f^{12}5s^25p$ | $4f^{12}5s5d$ | $4f^{11}5s5d$ |
| | $4f^{12}5s^25p^25d$ | $4f^{13}5s5p^2$ | $4f^{12}5s^25d$ | $4f^{11}5s^25p$ | $4f^{10}5s^25p$ |
| | | $4f^{13}5s5d^2$ | $4f^{12}5s5p^2$ | $4f^{11}5s^25d$ | $4f^{10}5s^25d$ |
| | | $4f^{13}5s5p5d$ | $4f^{11}5s^25p^2$ | $4f^{11}5s5p^2$ | |
| | | $4f^{12}5s^25p^2$ | | $4f^{10}5s^25p^2$ | |
| | | $4f^{12}5s^25p5d$ | | | |
| | | $4f^{12}5s^25d^2$ | | | |
| Ground state | $4f^{13}5s^25p^2\ ^4F_{7/2}$ | $4f^{14}5s^2\ ^1S_0$ | $4f^{13}5s^2\ ^2F_{7/2}$ | $4f^{12}5s^2\ ^3H_6$ | $4f^{11}5s^2\ ^4I_{15/2}$ |
| | $[(4f^{13})_{7/2}5s^2(5p^2_{1/2})_0]_{7/2}$ | $[4f^{14}5s^2]_0$ | $[(4f^{13})_{7/2}5s^2]_{7/2}$ | $\{[(4f^6_{5/2})_0(4f^6_{7/2})_6]_6 5s^2\}_6$ | $\{[(4f^6_{5/2})_0(4f^5_{7/2})_{15/2}]_{15/2}5s^2\}_{15/2}$ |

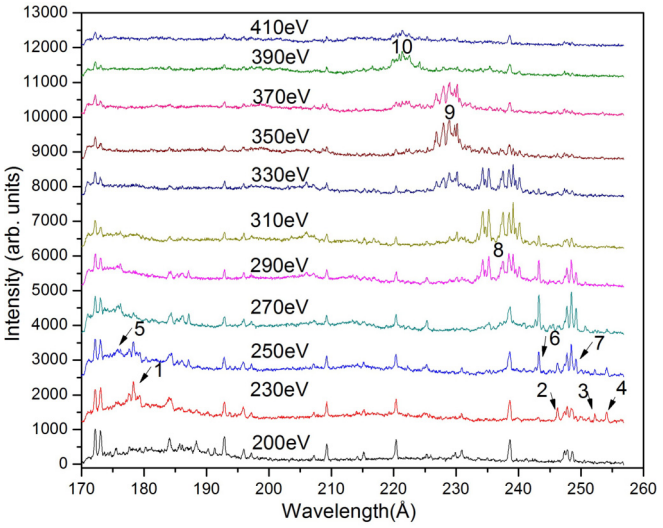


FIG. 1. (Color online) Spectra taken at SH-HtscEBIT at 11 electron-beam energies from 200 to 400 eV, with a beam current of 8.1 mA, while injecting $W(CO)_6$. Based on the ionization potentials given in Table III, the lines labeled 1, 2, 3, and 4 belong to $W^{11+}$ lines, and lines 5, 6, and 7 belong to $W^{12+}$ lines. Transition array 8 is from $W^{13+}$, transition array 9 is from $W^{14+}$, and transition array 10 is from $W^{15+}$.

To give models of reasonable complexities, we restricted our model to include configurations created by single and double excitation from $4f$, $5s$, and $5p$ subshells, as shown in Table II, where we also give the total number of states included for each ion. The synthetic spectra were created using CR models for beam energies of 230, 270, 310, 350 and 390 eV, respectively, for $W^{11+}$ to $W^{15+}$ at an electron density of $5 \times 10^{10}$ cm$^{-3}$, which is a typical electron density for the SH-HtscEBIT. The calculated lines are convolved with a Gaussian line shape to match the spectrometer resolution of 850.

## IV. RESULTS AND DISCUSSION

The measurements reported in this work spanned the wavelength region of 100–400 Å, but all identified lines fall in the 160–270 Å region. The spectral development as a function of electron-beam energy, and therefore the charge state of the tungsten ions, is shown in Fig. 1.

Based on the ionization potentials given in Table III, we assign the features labeled 1, 2, 3, and 4, which appear at electron-beam energies between 200 and 230 eV, to the spectrum of $W^{11+}$. In the same way, we conclude that the features labeled 5, 6, and 7 belong to $W^{12+}$ lines, transition array 8 is from $W^{13+}$, transition array 9 is from $W^{14+}$, and transition array 10 is from $W^{15+}$. The identification of the $W^{13+}$ arrays is further supported by the fact that they appear

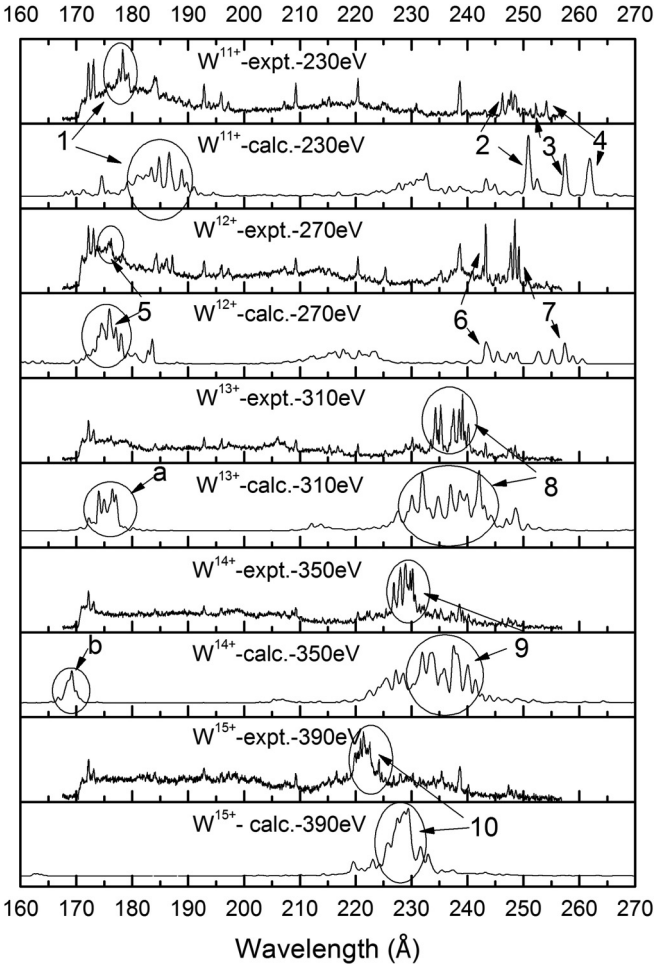


FIG. 2. Experimental (expt.) and synthetic (calc.) EBIT spectra of $W^{11+}$ to $W^{15+}$ at electron energies of 230, 270, 310, 350, and 390 eV. The calculated lines were convoluted with a linewidth to resemble an instrument resolution of 850. The numbers refer to the same transitions as in Fig. 1 and Table IV. Lines labeled a and b in the synthetic spectra are not possible to observe in the experiment due to the Al foil transmission properties (giving rise to the cutoff around 170 Å).

at the same beam energy as the visible lines in the same ion, as identified in [8]. In Fig. 2 we compare these experimental spectra with our synthetic ones from the CR-model spectra at some selected electron energies, where a single charge state dominates for each case. We also list our computed ground states of $W^{11+}$ to $W^{15+}$, which agree with earlier results by Kramida and Shirai [28].

The synthetic spectra give us important guidance when identifying the experimental results, but there are two clear and systematic deviations. First, there is a shift towards longer wavelengths in the calculations, and second, the transition

TABLE III. The ionization potential of $W^{11+}$ to $W^{15+}$ [28].

| | Charge state | | | | | |
|---|---|---|---|---|---|---|
| | $W^{10+}$ | $W^{11+}$ | $W^{12+}$ | $W^{13+}$ | $W^{14+}$ | $W^{15+}$ |
| Ionization energy (eV) | 208.9 ± 1.2 | 231.6 ± 1.2 | 258.2 ± 1.2 | 290.7 ± 1.2 | 325.3 ± 1.5 | 361.9 ± 1.5 |

TABLE IV. Identified lines and arrays in $W^{11+}$ to $W^{15+}$. The labels in the second column refer to Fig. 2. The wavelengths are in units of angstroms. The uncertainties of the experimental wavelengths in transition arrays are around 0.15 Å and are mainly due to the statistical uncertainty of the wavelength calibration and fitting.

| Ion | Label | Experimental wavelength | Theoretical wavelength | Transitions | Type |
|---|---|---|---|---|---|
| $W^{11+}$ | 1 | 175.6–180.4 | 183.3–189.0 | $4f^{13}5s^25p5d \rightarrow 4f^{13}5s^25p^2$ | array |
| | 2 | 246.23 ± 0.12 | 250.84 | $\{[(4f^{13})_{5/2}5s]_3(5p_{1/2}^2 5p_{3/2})_{3/2}\}_{3/2} \rightarrow \{[(4f^{13})_{5/2}5s^2]_{5/2}(5p_{1/2}^2)_0\}_{5/2}$ | line |
| | 3 | 252.25 ± 0.18 | 257.46 | $\{[(4f^{13})_{5/2}5s]_2(5p_{1/2}^2 5p_{3/2})_{3/2}\}_{7/2} \rightarrow \{[(4f^{13})_{5/2}5s^2]_{5/2}(5p_{1/2}^2)_0\}_{5/2}$ | line |
| | 4 | 254.09 ± 0.17 | 261.98 | $\{[(4f^{13})_{5/2}5s]_3(5p_{1/2}^2 5p_{3/2})_{3/2}\}_{5/2} \rightarrow \{[(4f^{13})_{5/2}5s^2]_{5/2}(5p_{1/2}^2)_0\}_{5/2}$ | line |
| $W^{12+}$ | 5 | 174.8–176.8 | 173.8–178.0 | $4f^{12}5s^25p5d \rightarrow 4f^{12}5s^25p^2$ | array |
| | 6 | 243.27 ± 0.13 | 243.29 | $\{[(4f^{13})_{7/2}5s]_4 5p_{1/2}]_{9/2}5p_{3/2}\}_4 \rightarrow [(4f^{13})_{7/2}5s^25p_{1/2}]_4$ | line |
| | 7 | 249.19 ± 0.13 | 257.43 | $\{[(4f^{13})_{7/2}5s]_3 5p_{1/2}]_{7/2}5p_{3/2}\}_5 \rightarrow [(4f^{13})_{7/2}5s^25p_{1/2}]_4$ | line |
| $W^{13+}$ | a | | 173.3–178.08 | $4f^{12}5s^25d \rightarrow 4f^{12}5s^25p$ | array |
| | 8 | 232.7–240.9 | 225.8–245.9 | $\begin{cases} 4f^{13}5s5p \rightarrow 4f^{13}5s^2 \\ 4f^{12}5s5p^2 \rightarrow 4f^{12}5s^25p \end{cases}$ | array |
| $W^{14+}$ | b | | 166.6-171.3 | $4f^{11}5s^25d \rightarrow 4f^{11}5s^25p$ | array |
| | 9 | 225.4–233.7 | 221.5–242.7 | $\begin{cases} 4f^{12}5s5p \rightarrow 4f^{12}5s^2 \\ 4f^{11}5s5p^2 \rightarrow 4f^{11}5s^25p \end{cases}$ | array |
| $W^{15+}$ | 10 | 214.8–226.9 | 218.4–234.5 | $4f^{11}5s5p \rightarrow 4f^{11}5s^2$ | array |

arrays are too wide in the synthetic spectra. It may be possible to correct for these differences by including more correlation, such as core-core (CC) correlation [11], but since we are aiming for CR modeling with a large number of atomic properties, we have to limit the size of our atomic structure model. It is clear, however, that the features of the synthetic spectra can be used to identify the transition arrays appearing for each of the tungsten charge states.

The lines are for all ions concentrated in the wavelength regions (see Fig. 2) 160–190 and 210–260 Å. The former corresponds to $5d \rightarrow 5p$ transitions, while the latter arises from $5p \rightarrow 5s$ arrays. The results are in agreement with Suzuki *et al.*'s work [29], in which their calculation showed $5p \rightarrow 5s$ transitions dominating the spectrum around 250 Å for the tungsten charge states of $W^{12+}$–$W^{15+}$. Our detailed identifications are listed in Table IV, and we will discuss them for each ion in detail in the following paragraphs.

*a.* $W^{11+}$. Our predicted ground state of $W^{11+}$ is $4f^{13}5s^25p^2$ ($\{[(4f_{5/2}^6)_0(4f_{7/2}^7)_{7/2}]_{7/2}5s^2(5p_{1/2}^2)_0\}_{7/2}$ in $jj$ coupling). The experimental and synthetic spectra are shown in Fig. 2 at $E = 230$ eV. According to the spectra, four transition arrays or lines are determined to be from this ion. $4f^{13}5s^25p5d \rightarrow 4f^{13}5s^25p^2$ transitions contribute to the 175.6–180.4 Å array (labeled 1 in Fig. 2) and the three longer-wavelength lines we identify as $4f^{13}5s5p^3 \rightarrow 4f^{13}5s^25p^2$ transitions.

*b.* $W^{12+}$. In the present work the ground state of $W^{12+}$ is $[4f^{14}5s^2]_0$. We also compared our computational results with available data in [30]. The differences between our RCI results and the various results from [30], i.e., first-order relativistic many-body perturbation theory (RMBPT1), second-order relativistic many-body perturbation theory (RMBPT2), and COWAN (a Hartree-Fock relativistic method) values of excitation energies, are 1%–5%, 0%–3%, and 1%–4%, respectively. Moreover, our results are in better agreement with the RMBPT2 results, and most of the excitation energies agree within 2%. We would like to point out that in spite of the fact that the ground state suggested from our calculations is the same as the ones given by Kramida and Shirai's and Safronova *et al.*'s works [28,30], this is only a tentative identification. The level splitting of the $4f^{12}5s^25p^2$ configuration is very sensitive to the computational model, and the inclusion of more correlation might push the lowest level in this configuration below the $4f^{14}5s^2\ ^1S_0$ level. A larger calculations will be needed to resolve this issue. The experimental and synthetic spectra are shown in Fig. 2 for an energy of $E = 270$ eV. Transition array 5 in the wavelength region of 174.8–176.8 Å in the experimental spectra (see Fig. 2) is identified as belonging to the $4f^{12}5s^25p5d \rightarrow 4f^{12}5s^25p^2$ array, while the other two lines at 243.3 and 249.2 Å are $5p \rightarrow 5s$ transitions, outside a $4f_{7/2}^{13}$ subshell.

*c.* $W^{13+}$. The experimental and synthetic spectra of this promethium-like ion are shown in Fig. 2 at $E = 310$ eV. There is still some remaining controversy concerning the ground state of $W^{13+}$ because of the effect of the "collapse" of the $4f$ orbital, which will lead to a change in ground-state configuration of promethium-like ions from $4f^{13}5s^2$ to $4f^{14}5s$, leading to a simpler semi-one-electron spectrum, with two strong resonance lines between the $5s$ and $5p$ levels (see Fig. 3). Curtis and Ellis predicted that this change would happen for $Z < 74$ by using the Hartree-Fork method [17]. Later, Theodosiou and Raftopoulos indicated that the change occurred first at $Z = 78$ by using the Dirac-Fork method [31]. Recent calculations [32–34] support the prediction of Theodosiou and Raftopoulos. Hutton *et al.* reported a detection of the $5p \rightarrow 5s$ resonance lines in a spectrum from the Berlin-EBIT [35], which would support the model by Curtis and Ellis, contradicting later theoretical predictions. However, the performance of this high-energy EBIT, working at only a few hundred eV energy, is quite debatable and leads to an uncertain and tentative identification.

The wavelengths of the $4f^{14}5p\ ^2P_{1/2} \rightarrow 4f^{14}5s\ ^2S_{1/2}$ and $4f^{14}5p\ ^2P_{3/2} \rightarrow 4f^{14}5s\ ^2S_{1/2}$ transitions for $W^{13+}$ are listed in Table V. In the present work our calculations predict the $4f^{14}5p\ ^2P_{1/2,3/2} \rightarrow 4f^{14}5s\ ^2S_{1/2}$ transition lines at 367.52

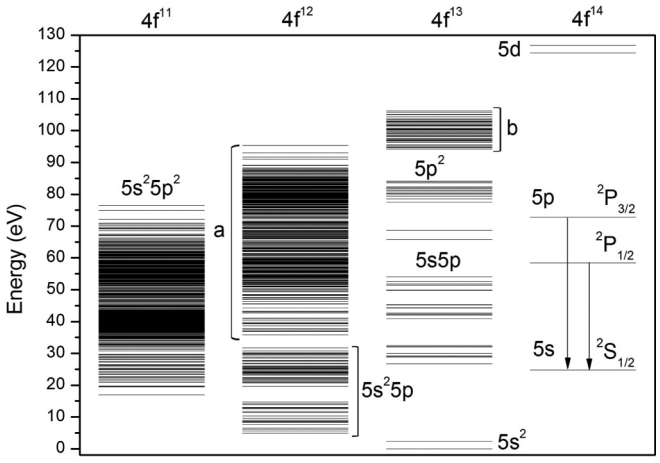


FIG. 3. Energy-level structure of $W^{13+}$. Here the label a refers to energy levels of the $4f^{12}5s^25d$ and $4f^{12}5s5p^2$ configurations, while the label b gives energy levels of $4f^{13}5s5d$ and $4f^{13}5p^2$. Lines of $W^{13+}$ observed in this work are mainly from the $4f^{12}5s^25d \rightarrow 4f^{12}5s^25p$, $4f^{13}5s5p \rightarrow 4f^{13}5s^2$, and $4f^{12}5s5p^2 \rightarrow 4f^{12}5s^25p$ transitions. The Curtis and Ellis [17] lines (see text) are marked on the right.

and 257.83 Å. The biggest difference between our RCI and other theoretical results for the $^2P_{1/2} \rightarrow {}^2S_{1/2}$ and $^2P_{3/2} \rightarrow {}^2S_{1/2}$ transitions are 0.96% and 1.27%, respectively. The difference between our RCI and the experimental results for the $^2P_{1/2} \rightarrow {}^2S_{1/2}$ and $^2P_{3/2} \rightarrow {}^2S_{1/2}$ transitions are 0.14% and 0.60%, respectively. The ground-state configuration is predicted to be $4f^{13}5s^2$, and our CR model does not indicate any strong $4f^{14}5p \rightarrow 4f^{14}5s$ lines. This is in agreement with our experiment, in which we did not observe any strong resonance line around the predicted position (see Table V) with a simple structure. Figure 3 shows the level structure of $W^{13+}$. Clearly, there are numerous levels lower in energy than $4f^{14}5s$ and $4f^{14}5p$. This leads to a low population of the $4f^{14}5p$ levels and hence weak lines as opposed to the strong lines predicted by Curtis and Ellis [17]. This situation is similar to that of $W^{11+}$ and $W^{12+}$, where the simplest configurations, with closed $4f^{14}$-subshell configurations, are not the ground state. The occurrence of simple spectra, with few resonance lines, will therefore occur for higher $Z$ in all the corresponding isoelectronic sequences. To further support the identification of $4f^{13}5s^2$ as the ground-state configuration of $W^{13+}$, we recently observed visible $M1$ transitions within the $4f^{13}5s^2$ and $4f^{12}5s^25p$ configurations using the SH-HtscEBIT [8]. Transition array 8 in Fig. 2 observed at around 232.7–240.9 Å was identified as $5p \rightarrow 5s$ arrays outside a $4f^{13}$ or $4f^{12}$ subshell (see Table IV), which coincide with the results of Safronova *et al.* [34]. A second strong transition array, labeled a in Fig. 2, positioned at 173.3–178.08 Å, arises from $5d \rightarrow 5p$ transitions, outside a $4f^{12}$ subshell, but is unobservable in the experimental spectrum due to the wavelength cutoff of the aluminium foil.

*d.* $W^{14+}$. We predict the ground state of $W^{14+}$ to be $4f^{12}5s^2$ ($\{[(4f^6_{5/2})_0(4f^6_{7/2})_6]_6 5s^2\}_6$ in $jj$ coupling). The experimental and synthetic spectra are shown in Fig. 2 at $E = 350$ eV. Transition array 9 in Fig. 2, covering the wavelength region of 225.4–233.7 Å, is suggested to be from $5p \rightarrow 5s$ transitions outside a $4f^{12}$ or $4f^{11}$ subshell (see Table IV). The shorter wavelengths labeled b in Fig. 2 at around the 166.6–171.3 Å wavelength region arises from $4f^{11}5s^25d \rightarrow 4f^{11}5s^25p$ transitions. Again, these lines did not appear in the experimental spectrum due to the Al foil transmission properties.

*e.* $W^{15+}$. Our predicted ground state of $W^{15+}$ is $4f^{11}5s^2$ ($\{[(4f^6_{5/2})_0(4f^5_{7/2})_{15/2}]_{15/2}5s^2\}_{15/2}$ in $jj$ coupling). The experimental and synthetic spectra are shown in Fig. 2 at $E = 390$ eV. Transition array 10 at 214.8–226.9 Å in Fig. 2 is identified as being from $4f^{11}5s5p \rightarrow 4f^{11}5s^2$.

## V. CONCLUSION

To conclude, we have studied EUV spectra from $W^{11+}$ to $W^{15+}$ ions experimentally and theoretically. The experiments were carried out using a flat-field spectrometer installed at the SH-HtscEBIT. The spectra were recorded at electron-beam energies ranging between 200 and 400 eV, and spectral features were recorded in the 170–260 Å region. In order to identify the charge states and spectral features we performed detailed RCI calculations of the relevant atomic structure. The data were then used in a CR model of the EBIT. Both calculations are a part of FAC. Although there were systematic shifts in the calculated wavelengths and the widths of the spectral features were systematically wider than the corresponding experimental arrays, the synthetic spectra are in good enough overall agreement with experiment to facilitate a number of identifications of arrays and lines. The spectral features in the 160–190 Å region are from $5d \rightarrow 5p$ transitions, whereas $5p \rightarrow 5s$ falls in the 210–260 Å region for all the ions considered. This work also identified the ground-state configuration of $W^{13+}$ as $4f^{13}5s^2$, supported by both experimental spectra and theoretical calculations.

TABLE V. Wavelength for the $4f^{14}5p\ ^2P_{1/2,3/2} \rightarrow 4f^{14}5s\ ^2S_{1/2}$ transitions in $W^{13+}$. The values are in units of angstroms.

| Transitions | RCI | RMBPT[a] | RMBPTB[b] | COWAN[c] | MR-MP[d] | Expt.[e] |
|---|---|---|---|---|---|---|
| $^2P_{1/2} \rightarrow {}^2S_{1/2}$ | 367.52 | 370.92 | 371.04 | 367.95 | 369.14 | 365.3 |
| $^2P_{3/2} \rightarrow {}^2S_{1/2}$ | 257.83 | 260.94 | 261.12 | 260.83 | 259.62 | 258.2 |

[a]Second-order approximation with Dirac-Fock potentials [34].
[b]Second-order approximation with Breit-Dirac-Fock potentials [34].
[c]Hartree-Fock relativistic method implemented in the COWAN code [34].
[d]Multireference Møller-Plesset approach [33].
[e]Experimental wavelengths from Ref. [35].

## ACKNOWLEDGMENTS

This work was supported by the Chinese National Fusion Project for ITER No. 2015GB117000 and Shanghai Leading Academic Discipline Project No. B107. W.L. is grateful for support from the Nordic Center at Fudan University for the exchange of staff between Fudan and Lund University.



[1] T. Pütterich, R. Neu, C. Biedermann, R. Radtke, and A. U. Team, J. Phys. B **38**, 3071 (2005).
[2] C. H. Skinner, Can. J. Phys. **86**, 285 (2008).
[3] V. Philipps, Phys. Scr. **T123**, 24 (2006).
[4] R. Barnsley (private communication).
[5] NIST Atomic Spectra Database, version 5, http://www.nist.gov/pml/data/asd.cfm.
[6] E. Träbert and P. Heekmann, Z. Phys. D **1**, 381 (1986).
[7] A. Kramida, Can. J. Phys. **89**, 551 (2011).
[8] Z. Zhao, M. Qiu, R. Zhao, W. Li, X. Guo, J. Xiao, Y. Zou, and R. Hutton, J. Phys. B **48**, 115004 (2015).
[9] W. Li, J. Xiao, Z. Shi, Z. Fei, R. Zhao, T. Brage, S. Huldt, R. Hutton, and Y. Zou, Phys. Rev. A (to be published), arXiv:1503.04523.
[10] Z. Fei, W. Li, J. Grumer, Z. Shi, R. Zhao, T. Brage, S. Huldt, K. Yao, R. Hutton, and Y. Zou, Phys. Rev. A **90**, 052517 (2014).
[11] Z. Fei, R. Zhao, Z. Shi, J. Xiao, M. Qiu, J. Grumer, M. Andersson, T. Brage, R. Hutton, and Y. Zou, Phys. Rev. A **86**, 062501 (2012).
[12] R. Zhao, J. Grumer, W. Li, J. Xiao, S. Huldt, T. Brage, R. Hutton, and Y. Zou, J. Phys. B **47**, 185004 (2014).
[13] J. Grumer, R. Zhao, T. Brage, S. Huldt, R. Hutton, and Y. Zou, Phys. Rev. A **89**, 062511 (2014).
[14] M. Qiu *et al.*, J. Phys. B **47**, 175002 (2014).
[15] Z. Shi, R. Zhao, W. Li, B. Tu, Y. Yang, J. Xiao, S. Huldt, R. Hutton, and Y. Zou, Rev. Sci. Instrum. **85**, 063110 (2014).
[16] M. F. Gu, Can. J. Phys. **86**, 675 (2008).
[17] L. Curtis and D. Ellis, Phys. Rev. Lett. **45**, 2099 (1980).
[18] J. Xiao, R. Zhao, X. Jin, B. Tu, Y. Yang, D. Lu, R. Hutton, and Y. Zou (unpublished).
[19] T. Kita, T. Harada, N. Nakano, and H. Kuroda, Appl. Opt. **22**, 512 (1983).
[20] T. Harada and T. Kita, Appl. Opt. **19**, 3987 (1980).
[21] T. Harada, K. Takahashi, H. Sakuma, and A. Osyczka, Appl. Opt. **38**, 2743 (1999).
[22] K. K. Lai and H. H. Lamb, Thin Solid Films **370**, 114 (2000).
[23] B. Edéln, Rep. Prog. Phys. **26**, 181 (1963).
[24] M. F. Gu, Phys. Rev. A **70**, 062704 (2004).
[25] M. F. Gu, Astrophys. J. Suppl. **156**, 105 (2005).
[26] M. F. Gu, T. Holczer, E. Behar, and S. M. Kahn, Astrophys. J. **641**, 1227 (2006).
[27] Y. Ralchenko, J. Phys. B **40**, F175 (2007).
[28] A. Kramida and T. Shirai, At. Data Nucl. Data Tables **95**, 305 (2009).
[29] C. Suzuki, C. S. Harte, D. Kilbane, T. Kato, H. A. Sakaue, I. Murakami, D. Kato, K. Sato, N. Tamura, S. Sudo, M. Goto, R. DArcy, E. Sokell, and G. O'Sullivan, J. Phys. B **44**, 175004 (2011).
[30] U. I. Safronova, A. S. Safronova, and P. Beiersdorfer, Phys. Rev. A **87**, 032508 (2013).
[31] C. E. Theodosiou and V. Raftopoulos, Phys. Rev. A **28**, 1186 (1983).
[32] A. Kramida and J. Reader, At. Data Nucl. Data Tables **92**, 457 (2006).
[33] M. J. Vilkas, Y. Ishikawa, and E. Träbert, Phys. Rev. A **77**, 042510 (2008).
[34] U. I. Safronova, A. S. Safronova, and P. Beiersdorfer, Phys. Rev. A **88**, 032512 (2013).
[35] R. Hutton, Y. Zou, J. R. Almandos, C. Biedermann, R. Radtke, A. Greier, and R. Neu, Nucl. Instrum. Methods Phys. Res., Sect. B **205**, 114 (2003).